Developmental Biology 373 (2013) 407–421

Contents lists available at SciVerse ScienceDirect

Developmental Biology

journal homepage: www.elsevier.com/locate/developmentalbiology

Modelling Delta-Notch perturbations during zebrafish somitogenesis

Philip J. Murray [a,*], Philip K. Maini [a,b], Ruth E. Baker [a]

[a] Centre for Mathematical Biology, Mathematical Institute, 24–29 St. Giles', Oxford OX1 3LB, UK
[b] Oxford Centre for Integrative Systems Biology, Department of Biochemistry, South Parks Road, Oxford OX1 3QU, UK

ARTICLE INFO

Article history:
Received 13 June 2012
Received in revised form
1 September 2012
Accepted 10 October 2012
Available online 16 October 2012

Keywords:
Somitogenesis
Delta-Notch signalling
Zebrafish
Salt and pepper
Clock and wavefront model
Mathematical model

ABSTRACT

The discovery over the last 15 years of molecular clocks and gradients in the pre-somitic mesoderm of numerous vertebrate species has added significant weight to Cooke and Zeeman's 'clock and wavefront' model of somitogenesis, in which a travelling wavefront determines the spatial position of somite formation and the somitogenesis clock controls periodicity (Cooke and Zeeman, 1976). However, recent high-throughput measurements of spatiotemporal patterns of gene expression in different zebrafish mutant backgrounds allow further quantitative evaluation of the clock and wavefront hypothesis. In this study we describe how our recently proposed model, in which oscillator coupling drives the propagation of an emergent wavefront, can be used to provide mechanistic and testable explanations for the following observed phenomena in zebrafish embryos: (a) the variation in somite measurements across a number of zebrafish mutants; (b) the delayed formation of somites and the formation of 'salt and pepper' patterns of gene expression upon disruption of oscillator coupling; and (c) spatial correlations in the 'salt and pepper' patterns in Delta-Notch mutants. In light of our results, we propose a number of plausible experiments that could be used to further test the model.

Introduction

Somitogenesis is the process by which the pre-somitic mesoderm (PSM) segments at regularly spaced time intervals into blocks of epithelial cells known as somites (Gilbert, 1997). Anterior somite production is accompanied by posterior growth and axis elongation, thus a posteriorly moving wavefront of differentiation is observed traversing the anterior–posterior (AP) axis of the vertebrate embryo. A molecular oscillator, known as the somitogenesis clock (Palmeirim et al., 1997), regulates the periodicity with which somites form, and a well accepted, though not directly measured, explanation for the observed patterns is that the clock oscillation rate attains its maximum value in the posterior PSM and decreases anteriorly along the AP axis. This gradient in oscillation rate results in narrowing waves of gene expression that travel anteriorly along the AP axis (see Fig. 1(a)). The somites then form in pairs, one on either side of the notochord, at the spatial positions where the oscillations cease.

Whilst snapshots of the expression patterns of clock genes (Fig. 1(a)) can be imaged using techniques such as *in situ* hybridisation (Jiang et al., 2000; Giudicelli et al., 2007), real-time expression assays, which have to date been performed for murine PSMs, allow the quantification of evolving patterns in a single experiment (Masamizu et al., 2006; Aulehla et al., 2008; Soroldoni and Oates, 2011, see Fig. 1(b) and (c)). Typically, the AP axis is plotted on the x-axis, with the origin represented by the position of a formed somite, time is represented on the y-axis and the signal intensity resulting from gene expression (e.g. fluorescence) is plotted on a colour scale. The space–time diagrams provide an intuitive way to visualise and quantify aspects of the clock and wavefront phenomenon. Moreover, analysis of real-time expression patterns can yield quantitative descriptions of quantities such as the propagating phase gradient or the pattern wavelength (see schematic in Fig. 1(d)) in individual experiments. We note that the short period of the segmentation clock ($\sim$30 min) in zebrafish embryos presents significant imaging challenges that have delayed the development of real-time expression assays (Soroldoni and Oates, 2011).

The observation that neighbouring oscillators are in phase (see, for example, Fig. 1(a)) is non-trivial as, given the inherent noise that must originate from factors such as cell heterogeneity, one might naively expect them to have slightly different oscillation rates, and hence to gradually drift out of phase with one another. During somitogenesis, and in many other biological contexts (*e.g.* Winfree, 1967; Strogatz, 2000), synchrony is maintained by oscillator coupling. In zebrafish, Delta-Notch signalling has been shown to play a fundamental role in the coordination of patterning in the posterior PSM (Özbudak and Lewis, 2008; Lewis et al., 2009).

Canonical Delta-Notch signalling is a receptor–ligand binding interaction in which the extracellular Delta ligand binds to the

* Corresponding author.
E-mail address: murrayp@maths.ox.ac.uk (P.J. Murray).

0012-1606/$ - see front matter © 2012 Elsevier Inc. All rights reserved.
http://dx.doi.org/10.1016/j.ydbio.2012.10.014

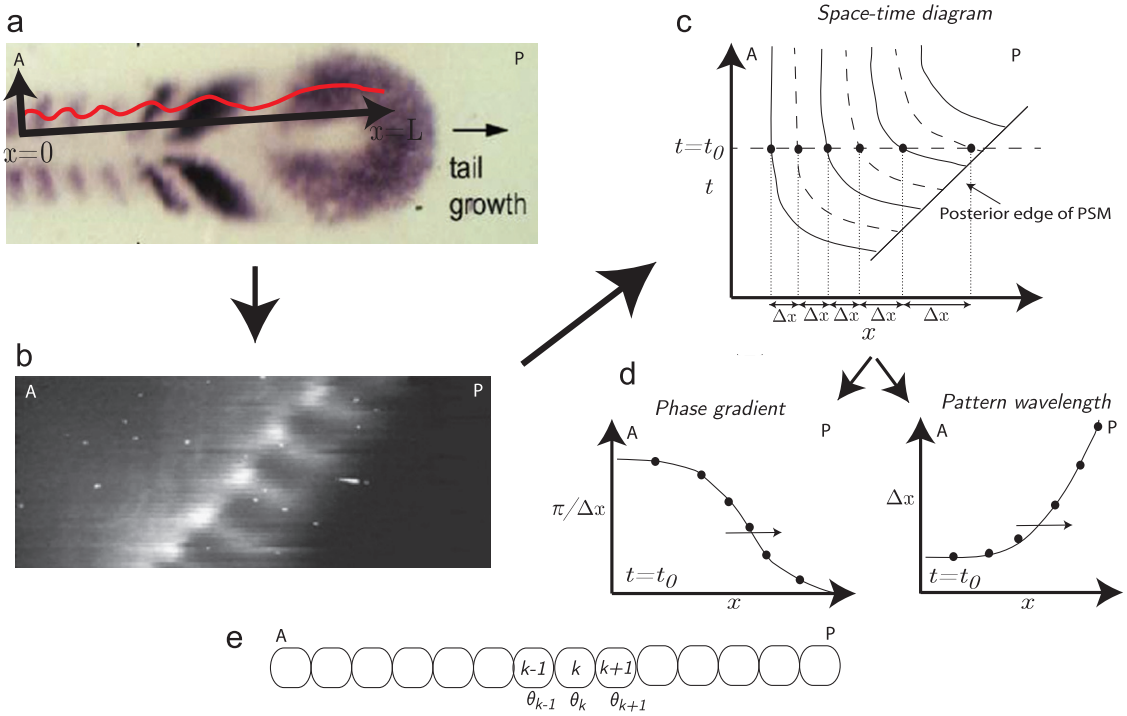

Fig. 1. (a) A zebrafish DeltaC *in situ* expression profile (Giudicelli et al., 2007) with a superimposed schematic of intensity peaks. (b) Real-time mouse clock expression patterns illustrated in a space–time diagram (Masamizu et al., 2006). Levels of gene expression (greyscale) are plotted against axial position and time. Copyright (2006) National Academy of Sciences, USA. (c) A schematic illustration of the fluorescence intensity plot presented in (b). The dashed line at $t=t_0$ represents a snapshot in time and the peaks and troughs are comparable to those depicted in (a). The markers, separated by spatial lengths Δx, along the dashed line represent increases in π in the phase of the pattern (i.e. peak to trough). (d) Using the space–time plot in (c), the phase gradient and pattern wavelength at $t=t_0$ can be approximated by $\pi/\Delta x$ and Δx, respectively. The arrow represents the posterior propagation of the profiles. (e) A schematic illustration of a one-dimensional chain of phase coupled oscillators aligned along the AP axis. Anterior (A) and posterior (P).

Notch receptor of a neighbouring cell, thus initiating transcriptional activity. In zebrafish there are four known members of the Delta family of Notch ligands and two active Notch receptors in the PSM. Upon binding of Delta ligands to Notch receptors, the Notch intracellular domain (NICD) is cleaved, allowing its transport to the nucleus, where it activates the transcription of target genes, including members of the hairy/enhancer of split (Her) family (Lewis et al., 2009). Transcriptionally regulated oscillations of the Her family play a fundamental role in generating oscillations (*e.g.* no somites form in double knockdowns of Her1 and Her7) and it is thought that members of the Her family may constitute the core somitogenesis oscillator (Oates and Ho, 2002). Hence in zebrafish, oscillations and the Delta-Notch mechanism of oscillator coupling are intrinsically connected.

The Tübingen zebrafish mutant screen (Van Eeden et al., 1996) yielded a number of mutants with a distinctive phenotype: only the anterior-most somites form as normal and, posterior to the last-formed somite, clock genes exhibit a 'salt and pepper' transcription pattern in which the levels of gene expression vary chaotically from cell to cell (Özbudak and Lewis, 2008). The mutant genes were labelled after eight (*aei*), deadly seven (*des*), beamter (*bea*) and mind bomb (*mib*) and, subsequently, each was found to be connected to the Delta-Notch signalling pathway: *aei* encodes for the DeltaD ligand, *des* for the Notch1a receptor, *bea* for the DeltaC ligand and *mib* for the E3 ubiquitin ligase, a protein that enables the Delta ligand to interact with the Notch receptor. The anterior limit of defects (ALD) phenomenon, which represents a quantification of the position of the last-formed somite (Riedel-Kruse et al., 2007), has previously been explained by a desynchronisation hypothesis in which the cumulative effect of noise in the absence of oscillator coupling is the breakdown of oscillator synchrony in the posterior PSM (Jiang et al., 2000; Horikawa et al., 2006; Riedel-Kruse et al., 2007; Özbudak and Lewis, 2008).

Many properties of the Delta-Notch mutants are observed upon application of the γ-secretase inhibitor DAPT (Geling et al., 2002), which prevents cleavage of NICD and hence its transport to the nucleus. Intriguingly, when DAPT is applied during somitogenesis, around 13 normal somites form before disruption; posterior to the last-formed somite, a 'salt and pepper' pattern is observed (Özbudak and Lewis, 2008; Riedel-Kruse et al., 2007). One expects the behaviour of DAPT-treated and Delta-Notch mutant embryos to be closely related but not identical owing to redundancies in the Delta-Notch signalling pathway.

The 'salt and pepper' patterns observed in the posterior PSM of Delta-Notch mutant and DAPT-treated embryos have recently been quantified using the spatial autocorrelation function

$$C_i(\delta) = \frac{1}{M}\sum_{j=1}^{M-\delta} I(x)I(x+\delta), \tag{1}$$

where $I(x)$ is the observed fluorescence intensity of cyclic gene expression at position x, M is the length of the spatial region over which the autocorrelation is calculated and δ is a length corresponding to the distance between two points in the PSM (Herrgen et al., 2010). The mean of the individual autocorrelation functions, $C(\delta)$, is calculated for a given batch of embryos by averaging over the C_i's at each value of δ. This formalism allows one to quantitatively compare noisy patterns across different perturbed embryos and thus, in principle, to distinguish between 'salt and pepper' patterns in different mutant embryos.

Mutants with weaker phenotypes offer further opportunities to investigate the interplay between the clock and wavefront. Hes6 (formerly Her13.2) is a member of the Her family of transcriptional regulators that has previously been identified as a potential molecular link between the somitogenesis clock and Fgf wavefronts (Kawamura et al., 2005). Schröter and Oates

(2010) constructed a Hes6 zebrafish mutant and measured the change, relative to wild-type embryos, in somitogenesis period, T_{exp}, and somite length, S_{exp}. In this experiment the mutant had a longer somitogenesis clock period, while the wavefront velocity was measured as having remained constant. Using a standard interpretation of Cooke and Zeeman's clock and wavefront model, the somite length is predicted to be the distance travelled by the wavefront in one cycle of the clock, *i.e.*

$$S_{exp} = vT_{exp}, \tag{2}$$

where v is the wavefront velocity. Intriguingly, and in agreement with Eq. (2), larger somites were observed in the mutant and somite length increased proportionally with the clock period.

In order to experimentally define the quantities in Eq. (2) in zebrafish embryos, time lapse imaging is used to determine the somitogenesis period whilst the position of the wavefront is assumed to be defined by the position of a stripe of gene expression that appears just prior to somite formation (Herrgen et al., 2010). Two distinctive methods of measuring anterior pattern wavelength in the PSM have been considered: somite length and segment length. The somite length is defined to be the distance between formed somites while the segment length is a more posterior measurement of pattern wavelength using the distance between consecutive stripes of mesp-b expression in the anterior PSM (Herrgen et al., 2010). Herrgen et al. (2010) propose that the more posterior measurement is superior as a host of anteriorly occurring processes, such as epithelialization, changes in packing, expression of adhesion and segment polarity molecules, muscle fibre elongation and somite shape and size changes, may influence the more anterior measurements. However, in modelling the clock behaviour the need to avoid describing the myriad of processes occurring in the anterior PSM must be balanced against the need to obtain a sufficiently anterior measurement of pattern wavelength such that the distance between the narrowing stripes of gene expression is sufficiently close to a steady-state value. Later we will see how this relatively subtle point can influence our interpretation of experimental measurements.

Reconciling somitogenesis models with recent observations

There is a rich history in the mathematical modelling of somitogenesis (see Baker et al., 2008 for a review). The clock and wavefront model (Cooke and Zeeman, 1976) is now widely accepted and used as a paradigm from which to explain the process of somitogenesis. The discovery of some of the governing molecular components of the clock and wavefront has led to the development of many molecular models of the clock in particular (see, for example, Hirata et al., 2002; Lewis, 2003; Goldbeter and Pourquié, 2008; Momiji and Monk, 2008). However, there are presumably many molecular constituents of the clock still undiscovered, and, even with those already identified, we cannot yet say precisely how they interact. Together with the ubiquitous problem of parameter identification, the result is that coarse-grained approaches are often taken (Kærn et al., 2000; Giudicelli et al., 2007; Riedel-Kruse et al., 2007; Morelli et al., 2009; Schröter and Oates, 2010; Ishimatsu et al., 2010; Murray et al., 2011) which can be used to investigate concepts such as cell–cell coupling and, in principle, link molecular models to tissue scale readouts of pattern formation.

The steady improvement in the quantification of somitogenesis motivates the refinement and development of existing modelling paradigms and in this study we ask whether our recently published clock and wavefront model of somitogenesis (Murray et al., 2011) can provide self-consistent and mechanistic explanations for a range of recent measurements of somitogenesis patterns in perturbed zebrafish embryos. We make a number of quantitative predictions about the zebrafish somitogenesis system that we hope can be used to both promote discussion and validate the assumptions on which our model relies.

Furthermore, our analysis has led us to two previously unexplained features of the most recently published data that are of general interest (Herrgen et al., 2010): firstly, Herrgen et al. (2010) have measured that the speed of the wavefront (defined using mesp-b stripe expression) is unchanged (relative to wild-type experiments) in the different Delta-Notch mutant and DAPT-treated embryos. Hence Eq. (2) predicts that the ratio of somite length to somitogenesis period should be unchanged in the perturbed embryos. As presented in Fig. 2(a), this is clearly not the case, regardless of whether somite length or segment length measurements are used to define S_{exp} in Eq. (2). Secondly, there is a peak in the autocorrelation functions of Delta-Notch mutant embryos at approximately four cell diameters (see Fig. 2(b)). We suggest that one would not expect a Gaussian noise in the phase dynamics, arising, for example, from transcriptional stochasticity in the somitogenesis clock, to yield the observed spatial frequencies, thus it appears unlikely that the mutant data supports a desynchronisation hypothesis in which transcriptional noise causes desynchronisation in the posterior PSM of Delta-Notch mutant embryos.

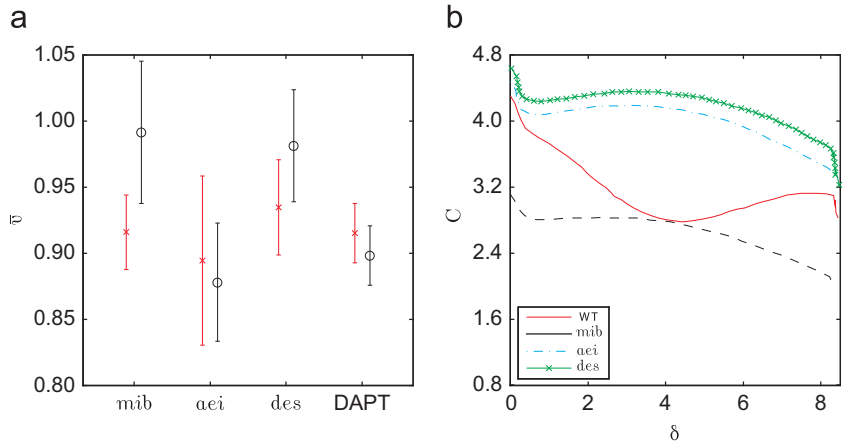

Fig. 2. (a) A plot of wavefront velocities (relative to wild type) for the *mib*, *aei*, *des* and DAPT-treated embryos. The velocities are calculated using measurements of anterior pattern wavelength, S_{exp}, and somitogenesis period, T_{exp}, from the perturbed embryos (Herrgen et al., 2010) and the formula $v = S_{exp}/T_{exp}$ (see Table 1 for values). Crosses and circles denote calculations made using somite and segment length measurements, respectively, as proxies for pattern wavelength. Error bars depict standard error of the mean. (b) Autocorrelation measurements from the anterior PSM of Delta-Notch mutant embryos. Data are replotted from Herrgen et al. (2010).

The layout of the paper is as follows: firstly, we briefly review the relevant results from our previous study (Murray et al., 2011); secondly, we parameterise the model using data from different Delta-Notch mutant strains; thirdly, we demonstrate how the model produces an ALD-like phenomenon upon the perturbation of cell–cell coupling; fourthly, we investigate mechanisms that could give rise to the peaked autocorrelation functions measured by Herrgen et al. (2010); and, finally, we conclude with a discussion of our main results.

Methods

Before moving on to the main topic of this paper, we introduce the reader to the most relevant details from our previous work (Murray et al., 2011) in which the progression of a cell through the segmentation clock cycle is modelled using a single variable, oscillator phase. Assuming symmetry of phase dynamics about the AP axis, we define the phase of the jth oscillator to be $\theta_j(t)$ (see Fig. 1(e)) and postulate the governing equations

$$\frac{d\theta_j}{dt} = \sum_i [A\sin(\theta_i-\theta_j)+B(\cos(\theta_i-\theta_j)-1)]+\omega, \tag{3}$$

where the sum is taken over nearest neighbours, ω is the natural oscillator frequency, A and B are the inter-cell coupling strengths, the oscillators reside on a fixed, discrete one-dimensional lattice and N is the number of oscillators in the system. The combination of attractive, sinusoidal coupling, which has a synchronising effect as it pushes the phases of neighbouring oscillators together, and cosine coupling results in a travelling gradient that slows the oscillation rate anteriorly. The sinusoidal coupling term represents the experimentally observed synchronising coupling between neighbouring oscillators mediated by juxtacrine signalling (Horikawa et al., 2006) while the cosine coupling term is a postulated, additional component of oscillator coupling (Murray et al., 2011).

Upon taking the continuum limit of Eq. (3) (see Appendix A), we obtain the partial differential equation

$$\frac{\partial\theta}{\partial t} = \omega + A\frac{\partial^2\theta}{\partial x^2} - B\left(\frac{\partial\theta}{\partial x}\right)^2, \tag{4}$$

and, motivated by the patterning profile observed in the *in situ* hybridisation presented in Fig. 1(a), we assume the boundary conditions

$$\left.\frac{\partial\theta}{\partial x}\right|_{x\to-\infty} = \sqrt{\frac{\omega}{B}}, \quad \left.\frac{\partial\theta}{\partial x}\right|_{x\to\infty} = 0, \tag{5}$$

In Fig. 3(b) we plot a snapshot of a periodic readout ($\sin\theta$) of the phase distribution that is qualitatively similar (compare with the schematic illustration of the expression intensity snapshot in Fig. 1(a)) to experimentally observed patterns of gene expression (spatial and temporal periodic oscillations behind and ahead of a moving wavefront, respectively). In Fig. 3(c) we plot a space–time diagram of the model solution that is conceptually equivalent to the real-time oscillatory gene expression patterns presented in

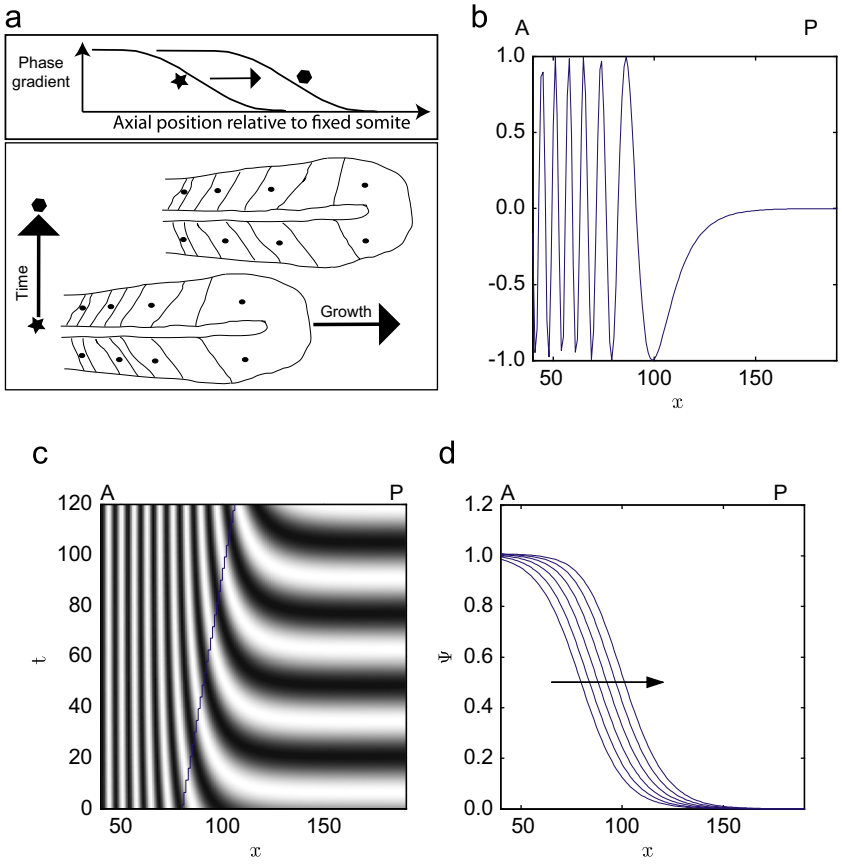

Fig. 3. Pattern propagation in a wild-type embryo. (a) A schematic illustration of snapshots of clock gene expression at consecutive time points. Posterior phase gradient motion is accompanied by PSM tip growth and oscillations in the tail. Dots denote the centre of a stripe of gene expression. (b)–(d) Plots of the numerical solution of Eqs. (4) and (5). Ahead of the wave (large x, small t) the pattern oscillates with period $2\pi/\omega$ in time but is spatially constant. Behind the wave (large t, small x) the pattern oscillates in space with wavelength S_{exp} but is constant in time. (b) A snapshot of phase patterns along the AP axis. $\sin\theta$ is plotted against x at $t=0$ min. Compare with Fig. 1(a). The dots in (a) correspond to the peaks in $\sin\theta$. (c) $\sin\theta$ plotted against x and t (black -1, white 1). The solid line denotes the position of the centre of the phase gradient. Compare with Fig. 1(b). (d) The phase gradient, Ψ, plotted against x at $t=\{0,20,40,60,80,100\}$ min. Compare with Fig. 1(d). See Table 2 for parameter values.

Fig. 1(b). We note that whilst the travelling wave nature of the solution is evident in the space–time plot, plotting the spatial gradient of the phase profile (Fig. 3(d)) provides an unambiguous definition of a travelling wavefront. Mathematical expressions for the phase gradient, $\Psi(x,t)$, and the pattern wavelength, $S(x,t)$, are provided in Appendix A.

An attractive feature of the model is that the parameters A, B and ω can be directly related to the experimental observables S_{exp}, L_{exp} and T_{exp} via the derived relationships

$$\omega = \frac{2\pi}{T_{exp}}, \quad B = \frac{S_{exp}^2}{2\pi T_{exp}}, \quad A = \frac{L_{exp}S_{exp}}{4T_{exp}}, \tag{6}$$

where L_{exp} is the length scale of the phase gradient, S_{exp} is the somite length and T_{exp} is the somitogenesis period (see Murray et al., 2011 for further details). Similarly, inverting the relationships in Eqs. (6) allows one to explain how changes to the model parameters A, B, and ω result in different values for the observables L_{exp}, S_{exp} and T_{exp}. We note that in our previous work (Murray et al., 2011) measurements from wild-type zebrafish embryos (Giudicelli et al., 2007) were used to determine, via Eqs. (6), the model parameters A, B and ω.

Given that measurements of somite length and somitogenesis period in Delta-Notch perturbed embryos indicate that Delta-Notch signalling can potentially influence wavefront velocities (see Fig. 2(a)), an attractive feature of the proposed model (Murray et al., 2011) is that somite size scales with the square root of oscillator period, *i.e.*

$$S_{exp} = \sqrt{2\pi B}\sqrt{T_{exp}}, \tag{7}$$

with the proportionality 'constant' dependent on the oscillator coupling strength B. Thus a mutation that increases the oscillator period, say, does not necessarily cause an increase in somite length. For example, if the mutation also sufficiently decreases B, then somite length could decrease even though the period has increased. Given that there is strong evidence that the somitogenesis clock is regulated by the Delta-Notch signalling pathway, it appears to be an entirely justifiable assumption that both the oscillator frequency and oscillator coupling could be influenced by a single mutation.

Later in this study we will investigate, within the context of the proposed model, the hypothesis that noise in the PSM is responsible for the ALD phenotype (Jiang et al., 2000; Riedel-Kruse et al., 2007; Özbudak and Lewis, 2008). Hence we introduce stochasticity into the discrete model (Eq. (3)) by including a Gaussian noise term and obtain

$$\frac{d\theta_j}{dt} = \sum_i [A\sin(\theta_i-\theta_j)+B(\cos(\theta_i-\theta_j)-1)]+\omega+D\zeta_j(t), \tag{8}$$

where $\zeta_j(t)$ represents a zero average un-correlated random noise of strength D. The additional noise term can be thought of as representing the effect of intrinsically stochastic subcellular processes, such as gene transcription. Simulation results (not shown) indicate that, so long as the noise strength is sufficiently small relative to the coupling parameter A, the addition of noise does not affect qualitative features of the simulation results. We will return to the discrete stochastic model later.

Results

Having introduced the key features of our recently proposed clock and wavefront model (Murray et al., 2011), we now investigate how the model can be used to provide novel, mechanistic and quantitative explanations of phenomena observed upon disruption of Delta-Notch signalling in zebrafish embryos.

Parameterising the model using measurements from different mutant strains

Variation in somite length and somitogenesis period has previously been quantified (Schröter and Oates, 2010; Herrgen et al., 2010) in a range of perturbed embryos (*aei*, *bea*, *des*, *mib* DAPT-treated, and Hes6) (see Table 3) and in this section we use Eqs. (6) to determine corresponding model parameters in each of the different cases. Subsequently, we discuss the biological significance and plausibility of the results.

For notational convenience, we define wild-type (S_{WT}, L_{WT}, T_{WT}) and mutated (S_M, L_M, T_M) experimental measurements, and associated model parameters (A_{WT}, B_{WT}, T_{WT}) and (A_M, B_M, T_M), respectively. Letting barred variables represent the ratios of mutated to wild-type parameters, the relative changes in model parameters in the different mutants can be written, upon manipulation of Eqs. (6), in terms of the relative changes in observed measurements as follows:

$$\overline{B} = \frac{\overline{S}^2}{\overline{T}}; \quad \overline{\omega} = \frac{1}{\overline{T}}; \quad \overline{v} = \frac{\overline{S}}{\overline{T}}. \tag{9}$$

A slowed oscillation rate and increased repulsive coupling strength can explain the Hes6 mutant phenotype

Schröter and Oates (2010) constructed a Hes6 mutant embryo and found that it has a segmentation clock period which is lengthened by $\sim 7\%$ relative to a wild-type embryo, somites are 7% bigger and the wavefront in the mutant embryo progresses at the same rate as in the wild-type embryo (see Table 3). As axis elongation speed is unaltered, fewer, larger, somites form in the mutant embryo. This observation fits the scaling relationship between somite length and oscillator period predicted by Cooke and Zeeman's clock and wavefront model (Eq. (2)), but can it be reconciled with the relationship predicted by our model (Eq. (7))?

If the parameter B changes in inverse proportion to the parameter ω in the Hes6 mutant, the somite length, $S_{exp} \propto \sqrt{B/\omega}$, increases while the wave speed, $v \propto \sqrt{\omega B}$, remains constant. If our model is correct, Hes6 both accelerates the clock and inhibits repulsive coupling, *i.e.* the repulsive coupling strength has an inverse dependence on the clock oscillation rate (see Table 3). Thus, in the absence of Hes6, the clock slows (ω decreases) and repulsive coupling is increased (B increases).

Somite length measurements imply that repulsive coupling is independent of canonical Delta-Notch signalling

Herrgen et al. (2010) used measurements of both somite and segment length to define pattern wavelength in the anterior PSM. As the measurement of pattern wavelength affects, via Eq. (9), the inferred value for the repulsive coupling strength, the differences in the measurements of pattern wavelength matter when one attempts to compare our model with the experimental observations.

Using the segment length data as a measurement of S_{exp}, in Fig. 4(a) we plot the Herrgen et al. (2010) measurements in $\overline{S}-\overline{T}$ space. Clearly, the DAPT-treated and *aei* mutant embryos can be grouped together and do not lie on the line where the relationship given by Eq. (2) holds. In contrast, using the somite length measurements, the DAPT-treated, *mib* and *aei* mutant embryos can be grouped together and have a different phenotype to both the Hes6 and *des* mutants. The differences between the measurement protocols are clearly indicated in Fig. 2(a) where we compare wavefront velocities.

It is not well understood what mechanisms underly the observations in the different mutants, nor is it clear whether the segment or somite measurements provide the more faithful representation of pattern wavelength in a given mutant. The conflict between

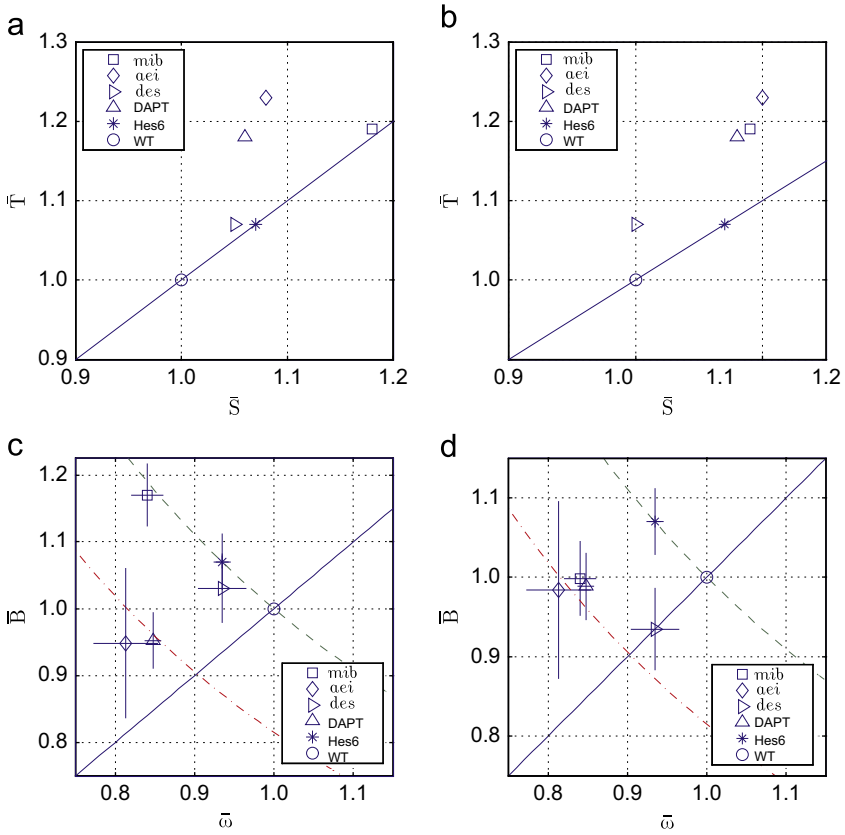

Fig. 4. Top row: plot of the Herrgen et al. (2010) segment (*left*) and somite (right) measurements in $\overline{S}-\overline{T}$ parameter space. The solid line is a line with constant wave speed. Bottom row: segment (*left*) and somite (*right*) measurements (Herrgen et al., 2010) are used in Eqs. (9) to identify the positions of the perturbed embryos in $\overline{\omega}-\overline{B}$ parameter space. The parameter space is divided into four quadrants by the solid line $\overline{B}=\overline{\omega}$ (constant somite length) and the dashed line $\overline{B}=1/\overline{\omega}$ (constant wave speed). When $\overline{B}>\overline{\omega}$ (above solid line) larger somites are obtained. If $\overline{B}<1/\overline{\omega}$ (below dashed line) the wave speed is reduced.

measurements is perhaps best illustrated by the *mib* mutant: the segment and somite measurements suggest unchanged and reduced wavefront velocities, respectively.

Using Eqs. (9) we can attempt to address some of these issues by relating the Herrgen et al. (2010) measurements to the phenomenon of oscillator coupling in our model (see Table 3 for numerical values) and the mutants can be interpreted in a corresponding $\overline{\omega}-\overline{B}$ parameter space (see Fig. 4(c) and (d)). This approach allows us to provide mechanistic explanations for the mutant measurements and to determine, at least within the context of the proposed model, whether segment or somite measurements are more appropriate.

In Fig. 4(c) we use the segment length data to plot the mutants in $\overline{\omega}-\overline{B}$ parameter space. Notably, when Eq. (2) holds (*mib*, Hes6 and *des* mutants), a decrease in oscillator frequency is accompanied by a proportional increase in repulsive coupling strength and the wave speed remains approximately constant. However, in the *aei* and DAPT-treated embryos, the decrease in oscillator frequency is accompanied by a decrease in the repulsive coupling strength. In summary, when interpreted in our model framework, it is not clear why the Delta-Notch mutants are separated in parameter space and we conclude that analysis of the perturbed embryos in $\overline{\omega}-\overline{B}$ parameter space does not lend any additional insight into potential mechanisms underlying the measurements made by Herrgen et al. (2010).

In Fig. 4(d) we use the somite length data to plot the mutants in $\overline{\omega}-\overline{B}$ parameter space. Notably, the *aei*, *mib* and DAPT-treated embryos all show a decrease in oscillator frequency with no change in the repulsive coupling strength. This observation permits the insight that repulsive coupling is not mediated via canonical Delta-Notch signalling. In contrast, the *des* mutant shows a decrease in the repulsive coupling strength. As *des* encodes for the notch1a receptor, we interpret this result as follows: repulsive coupling is partially mediated by the notch1a receptor but not via the canonical Delta-Notch signalling pathway. In summary, the somite length data permit an intuitive description of the Delta-Notch mutant measurements in which repulsive coupling is independent of canonical Delta-Notch signalling but dependent on the notch1a receptor.

Reduced phase gradient velocity hypothesis supported by mib mutant embryo expression data

Whilst the parameter space analysis in the previous section represents a novel method of analysing Delta-Notch mutant measurements, a comparison of clock gene expression profiles between wild-type and perturbed embryos should allow the hypothesis that phase gradient velocities are reduced in some Delta-Notch embryos to be tested directly.

For instance, after a time τ, or when N somites have formed in the wild-type embryo, perturbed and wild-type wavefronts will be separated by a distance

$$x_\tau=(1-\overline{v})\sqrt{\omega\overline{B}}\tau=(1-\overline{v})NS_{exp}, \tag{10}$$

where $\overline{v}$ is the relative change in the wavefront velocity (see Table 3). Thus at the four somite stage in the *mib* mutant, say, one expects, using the somite length data, a relatively small lag of

$$(1-\overline{v})\frac{S_{exp}}{T_{exp}}4T_{exp}=0.08\times 4.0=0.32, \tag{11}$$

somite lengths in the mutant embryo relative to the wild-type (using *mib* data from Table 3). In contrast, using the segment

length data the wavefront velocity in the *mib* mutant embryo is the same as in the wild-type case (see Fig. 2(a)).

This clear quantitative prediction can be tested by comparing measurements of pattern wavelength in wild-type and *mib* mutant embryos at the four somite stage (see Fig. 5 where data are reproduced from Herrgen et al., 2010). In the Appendix (Eq. (21)) we have shown that an expression for the pattern wavelength, the quantity that Herrgen et al. (2010) have directly measured, is given by

$$S(y)=2\pi\sqrt{\frac{B_{mib}}{\omega_{mib}}}\left(1+\frac{A_{mib}}{\pi B_{mib}}\sinh^{-1}\left(\sinh\left(\frac{\pi B_{mib}}{A_{mib}}\right)\times\exp\left(\frac{\sqrt{\omega_{mib}B_{mib}}}{A_{mib}}(y-c_2)\right)\right)\right). \quad (12)$$

The parameters B_{mib} and ω_{mib} have already been determined, using Eqs. (9), in the previous section but the parameters A_{mib} and c_2 cannot be explicitly determined so we fit them to the Herrgen et al. expression measurements using a least squares fitting algorithm. We find that A_{mib} and c_2 take the values (1.76, 0.308) and (1.58, 0.263) when fitted to the wild-type and mutant data, respectively (see Fig. 5). Hence, the best-fit value of A_{mib} is less than that of the wild-type embryo, indicating a steeper wavefront (+10%), while the centre of the phase gradient is shifted anteriorly by an amount $0.046L_{PSM}/S_{exp}=0.28$ (after rescaling to units of somite lengths) in the mutant. The residual mean-squared error is 0.07. Thus a least-squares fit of our model to the *mib* stripe expression data is consistent with the prediction of a reduced phase gradient velocity and hence the somite length measurements. We highlight that the prediction of phase gradient slowing could be further validated by analysis of clock gene expression patterns in DAPT-treated embryos.

Phase gradient steepening and stalling upon removal of diffusive coupling

As it is well accepted that canonical Delta-Notch signalling plays a crucial role in oscillator coupling in the PSM, and we have deduced that repulsive oscillator coupling is independent of canonical Delta-Notch signalling, we now make the assumption that canonical Delta-Notch signalling is represented in our model by the parameter A. Hence, in order to simulate Delta-Notch mutant and DAPT-treated embryos, we set $A=0$.

A well-studied feature of Eq. (4) in this case is that, upon removal of attractive coupling (diffusion), the gradient continues to propagate but steepens (see Fig. 6) until it eventually stalls after a finite time (see Appendix B for the derivation of this standard result). This phenomenon is therefore a key testable prediction of the proposed clock and wavefront model: phase gradient steepening upon treatment of zebrafish embryos with DAPT. Such a finding, which would be immediately apparent in real-time expression profiles of a DAPT-treated embryo, would provide strong evidence that canonical Delta-Notch signalling is not the only mechanism of oscillator coupling in the zebrafish somitogenesis system.

Whilst it is an attractive hypothesis that the stalling of the phase gradient might significantly contribute to the ALD phenomenon, we highlight that Riedel-Kruse et al. (2007) have found that 11 further somites (accounting for a two somite pharmacological delay) form upon treatment of wild-type zebrafish embryos with DAPT solution. In contrast, the time taken for stalling of the phase gradient in our model corresponds to the formation of

$$N_s=\frac{4A}{\sqrt{\omega B}}=\frac{L_{exp}}{S_{exp}}\sim 6, \quad (13)$$

somites (wild-type zebrafish embryo with parameter values taken from Table 2).

If phase gradient steepening contributes towards ALD, we suggest three plausible hypotheses that might explain the underestimate in Eq. (13): (a) our model derivation is based upon the assumption of constant cell density along the AP axis. Whilst we are not aware of direct measurements in zebrafish, Bénazéraf et al. (2010) have observed, in chick embryos, that there is a posteriorly decreasing density gradient along the AP axis, with the density decreasing by a factor of two posteriorly. If such a density gradient were found in zebrafish, the method by which we currently fit Eq. (21) to the stripe expression data (e.g. Fig. 5) would result in an underestimate of the parameter A. Subsequently, our prediction for the number of somites that form after disruption of attractive coupling (see Eq. (13)) would be an underestimate. Thus a posteriorly decreasing density gradient might account for a number of the missing somites in the current model; (b) the parameter A might tend to zero over some finite

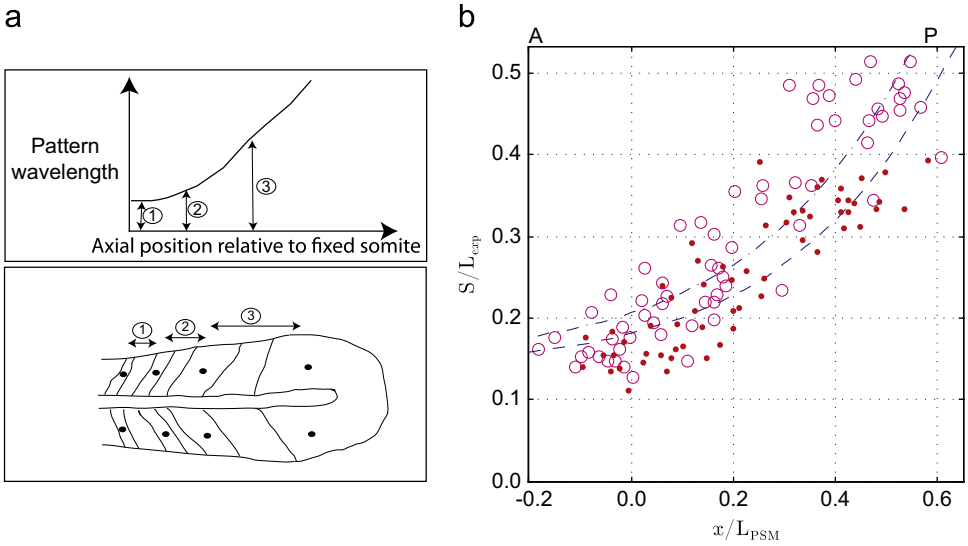

Fig. 5. Comparison of stripe expression patterns between wild-type and mutant embryos provides evidence for altered phase gradient velocities in mutant embryos. (a) A schematic illustration of the measurement of inter-stripe distance (pattern wavelength) as a function of axial position. (b) Least squares fits of Eq. (12) to the Herrgen et al. (2010) stripe expression data from both wild-type (dots, dashed line) and *mib* (circles, dot dashed line) mutant embryos are consistent with a phase gradient lag in the mutant embryo. The distance between stripes of gene expression is plotted against position along the AP axis.

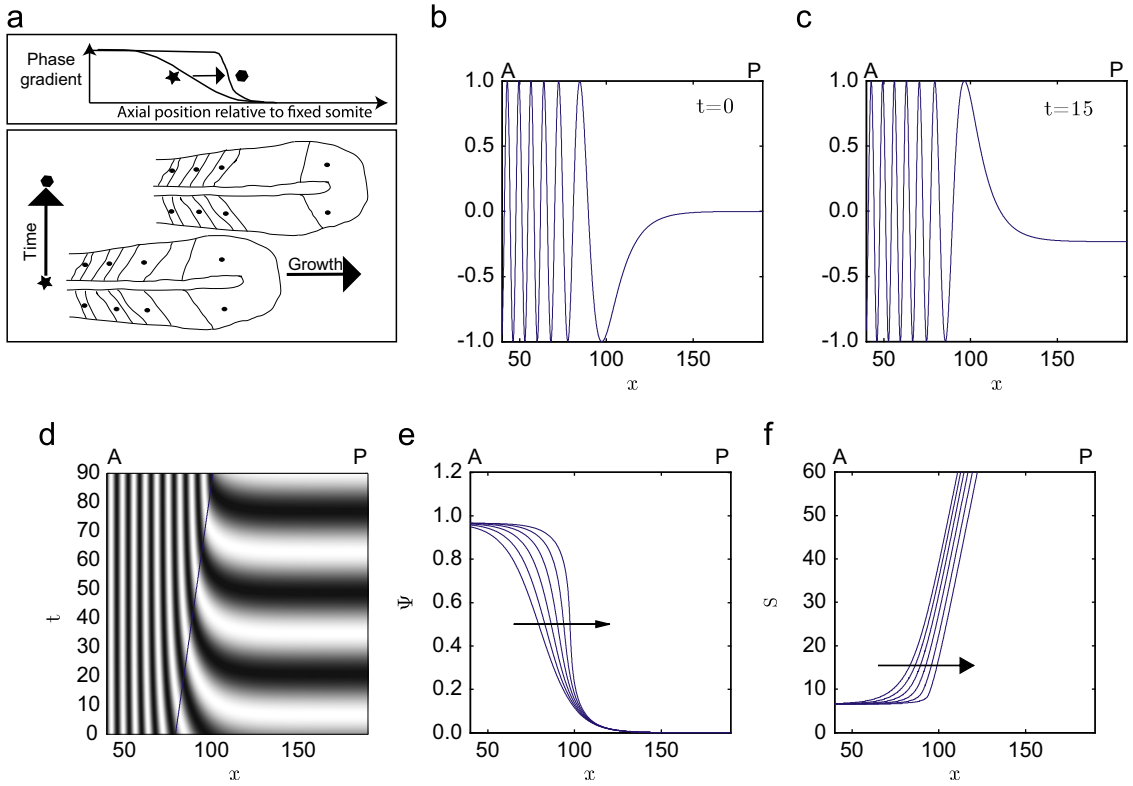

Fig. 6. The continuum model predicts phase gradient steepening and stalling upon removal of diffusive coupling. (a) A schematic illustration of the predicted phase gradient steepening upon embryo treatment with DAPT solution. (b)–(f) Eqs. (4) and (5) were solved with the parameter A set to zero at $t=0$. The wavefront steepens for $0<t<t_s$ and eventually stalls at $x=100$. (b)–(c) Snapshots of oscillation pattern plotted along the AP axis. $\sin\theta$ is plotted against x at $t=\{0,15\}$ min. (d) A space–time illustration of phase dynamics. $\sin\theta$ plotted against x and t (black -1, white 1). (e) The phase gradient, Ψ, is plotted against axial position, x, at $t=\{0,15,30,45,60,75\}$ min. (f) S plotted against x at $t=\{0,15,30,45,60,75\}$ min. Note the bilinear profile as $t\to t_s$ (see Appendix B). The spatial coordinate, x, in the laboratory frame, increases posteriorly. See Table 2 for parameter values and Fig. 1 for comparable experimental figures.

Table 1
A table summarising the observed effect of somitogenesis perturbations. $\overline{T}$ – fractional change in somitogenesis period relative to wild-type; $\overline{S}$ – fractional change in segment length relative to wild-type; $\overline{S^{\dagger}}$ – fractional change in somite length relative to wild-type; ALD – anterior limit of defects. Data (mean $\pm$ 95% confidence intervals) taken and replotted from Schröter and Oates (2010) and Herrgen et al. (2010).

Observation	Hes6	*mib*	*aei*	*des*	DAPT
Salt and pepper	N	Y	Y	Y	Y
ALD	N/A	10–12	7–9 $\pm$ 2	7–9 $\pm$ 2	18 $\pm$ 0.2
$\overline{T}$	1.07 $\pm$ 0.01	1.19 $\pm$ 0.02	1.23 $\pm$ 0.04	1.07 $\pm$ 0.03	1.18 $\pm$ 0.01
$\overline{S}$	N/A	1.18 $\pm$ 0.05	1.08 $\pm$ 0.02	1.05 $\pm$ 0.03	1.06 $\pm$ 0.02
$\overline{S}^{\dagger}$	1.07 $\pm$ 0.02	1.09 $\pm$ 0.02	1.10 $\pm$ 0.05	1.0 $\pm$ 0.02	1.08 $\pm$ 0.02

Table 2
A description of the model parameters.

Parameter	Definition	Value	Unit
A	Attractive coupling strength	2.32	c.d.^{2}/min
B	Repulsive coupling strength	0.24	c.d.^{2}/min
ω	Oscillation frequency	0.22	min^{-1}
L_{exp}	PSM length	40	c.d.
S_{exp}	Somite length	6.5	c.d.
T_{exp}	Somitogenesis period	28	min
v	Wavefront velocity	S_{exp}/T_{exp}	c.d./min
D	Noise strength	0.02	min^{-1}
N	Number of cells in discrete simulations	200	Nondim

c.d. (cell diameters).

time rather than instantaneously; and (c) as the phase gradient steepens, the length scale over which it varies tends to that of a single cell and the continuum model is no longer an accurate description of cellular phase dynamics (see Fig. 7 and Appendix B). In each case, Eq. (13) can be viewed as a lower bound on the number of somites that can form.

Phase gradient steepening in the discrete stochastic model reproduces ALD but not autocorrelation measurements

Motivated by the hypothesis that the discrete nature of cells in the PSM may become important as the length scale over which the phase gradient varies tends to that of a single cell, we now explore behaviour in the discrete model (Eqs. 3) when $A=0$. We again find that the phase gradient steepens, as in the continuum case, but continues to propagate (see Fig. 7), thus allowing for the potential for further somite formation beyond the six predicted by the continuum model analysis. Thus the discrete model with $A=0$ predicts that somite formation continues unbounded, a result that is again not in agreement with the observations of Riedel-Kruse et al. (2007).

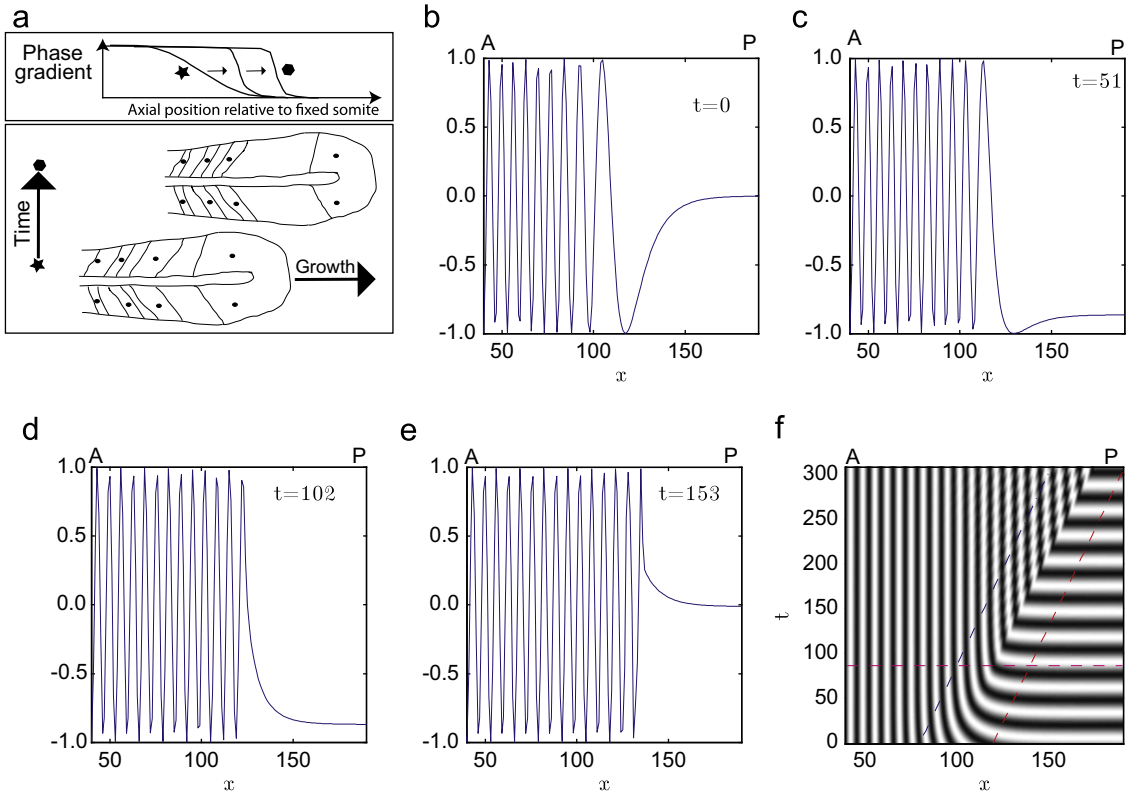

Fig. 7. The discrete model predicts phase gradient steepening but continued pattern formation upon removal of diffusive coupling. (a) A schematic illustration of the predicted effect. (b)–(f) Equations (3) and (5) were solved with the parameter A set to zero at $t=0$. Note the continued propagation of pattern after $t=t_s$ (see Appendix B). (b)–(e) $\sin\theta$ plotted against x at $t=\{0,51,102,154\}$ min. (f) $\sin\theta$ plotted against x and t (black -1, white 1). The spatial coordinate in the laboratory frame, x, increases posteriorly.
See Table 2 for parameter values.

Table 3
Changes in somite length and somitogenesis period in different mutants relative to wild-type (Herrgen et al., 2010) and the corresponding changes in the model parameters B and ω (barred notation represents fractional change with respect to wild-type values). See Fig. 4 for a graphic illustration of these data.

Observation	Hes6	*mib*	*aei*	*des*	DAPT
$\overline{T}$	1.07 ± 0.01	1.19 ± 0.02	1.23 ± 0.04	1.07 ± 0.03	1.18 ± 0.01
$\overline{S}$	1.07 ± 0.02	1.09 ± 0.02	1.10 ± 0.05	1.0 ± 0.02	1.08 ± 0.02
$\overline{B}$	1.09 ± 0.04	1.10 ± 0.04	1.00 ± 0.11	1.08 ± 0.05	1.07 ± 0.04
$\overline{B}^{\dagger}$	1.07 ± 0.04	1.00 ± 0.04	0.98 ± 0.11	0.93 ± 0.05	0.99 ± 0.04
$\overline{\omega}$	0.93 ± 0.01	0.84 ± 0.02	0.81 ± 0.04	0.93 ± 0.03	0.85 ± 0.01
$\overline{v}$	1.0 ± 0.03	0.92 ± 0.02	0.90 ± 0.06	0.93 ± 0.04	0.92 ± 0.02

However, when $A=0$ we expect stochasticity in the clock dynamics to play a fundamental role in pattern formation, as there is no longer synchronisation between neighbouring oscillators. We now investigate whether the discrete stochastic model (Eqs. (8)) can reproduce a standard explanation for the ALD phenomenon: noise in the absence of oscillator coupling results in neighbouring oscillators randomly drifting out of phase until the clock pattern is completely disrupted in the posterior PSM (Jiang et al., 2000; Riedel-Kruse et al., 2007). The addition of noise to the discrete phase dynamics has little qualitative effect when wild-type parameters are used (results not shown) as the diffusive coupling smooths out stochastic fluctuations. However, in the limit $A=0$ there is no homogenising term to counteract the destabilising effects of noise and repulsive coupling, and neighbouring oscillators in the posterior PSM eventually drift out-of-phase . The combination of noise and repulsive coupling is sufficient to completely disrupt the formation of a regular pattern (see Fig. 8). Hence, the discrete stochastic model appears to have all the ingredients necessary to recapitulate the ALD observations in DAPT-treated and Delta-Notch mutant embryos.

However, there is one further set of data that can be used to validate models of ALD: the autocorrelation measurements made by Herrgen et al. (2010) in Delta-Notch mutant embryos (see Fig. 2(b)). Following Herrgen et al. (2010), we equate fluorescence intensities with the sine of the phase ($I(x)=\sin(\theta(x))$) and our simulation results confirm what one might expect intuitively: the autocorrelation function shows no intermediate peak (see Fig. 9(c)) and is indistinguishable from the autocorrelation function of a population of oscillators with randomly distributed phases. Thus, in our model, the experimentally observed autocorrelation function cannot be reproduced by a Gaussian noise term representing intrinsic noise in the somitogenesis clock and the unanswered question remains: what mechanism can give rise to the peaked autocorrelation function measured by Herrgen et al. (2010)?

M phase block of somitogenesis clock yields phase lags consistent with peaked autocorrelation functions

Having found that the discrete stochastic model cannot reproduce the peaked autocorrelation function measured by Herrgen et al. (2010), we sought an alternative mechanism. Recalling Horikawa et al.'s observation that a cell's somitogenesis clock is paused during M phase of the cell cycle, with the consequence that a mother-daughter cell pair lag neighbouring cells upon M phase exit (Horikawa et al., 2006), we deduced that M phase block might be responsible for peaked autocorrelation functions and hence play a role in the generation of 'salt and pepper' patterns in Delta-Notch mutants.

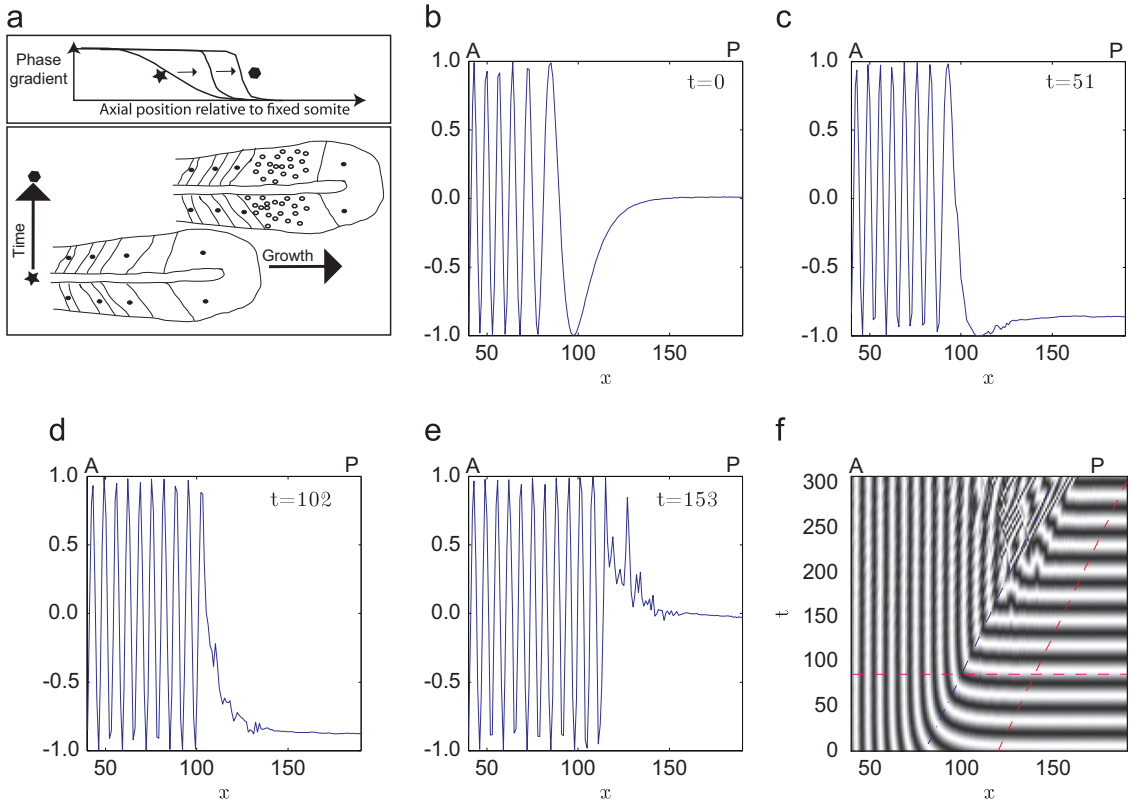

Fig. 8. The discrete stochastic model predicts phase gradient steepening, limited somite formation and 'salt and pepper' patterns. (a) A schematic illustration of the predicted effect. (b)–(f) Eqs. (8) and (5) were solved with the parameter A set to zero at $t=0$. Note the emergence of the 'salt and pepper' pattern ahead of the wavefront. (b)–(e) $\sin\theta$ plotted against x at $t=\{0,51,102,153\}$ min. (f) $\sin\theta$ plotted against x and t (black -1, white 1). The spatial coordinate in the laboratory frame, x, increases posteriorly. See Table 2 for parameter values.

We reasoned that in Delta-Notch mutant and DAPT-treated embryos, the ability of the phase differences induced by M phase block to dissipate is lost and the relative lengths of M phase of the cell cycle and the period of the somitogenesis clock could gradually induce a new spatial periodicity into the oscillator population, as, after M phase of the cell cycle, a divided cell in the posterior-most PSM will be out-of-phase with neighbouring cells by an amount given by

$$\Delta\theta = 2\pi\frac{T_M}{T_{exp}}. \tag{14}$$

However, as the maximum observable phase difference between a pair of oscillators is π, we define the measurable phase difference using the 'hat' function

$$\overline{\Delta\theta} = \begin{cases} 2\pi\dfrac{T_M}{T_{exp}} & \text{if } \dfrac{T_M}{T_{exp}} < \dfrac{1}{2}, \\ 2\pi\left(1-\dfrac{T_M}{T_{exp}}\right) & \text{if } \dfrac{1}{2} < \dfrac{T_M}{T_{exp}} < 1. \end{cases} \tag{15}$$

In a population of oscillators separated in phase by an amount $\overline{\Delta\theta}$, we expect an observed spatial periodicity (*i.e.* a peak in the autocorrelation function) at wavelength

$$S_M = 2\pi/\overline{\Delta\theta} = \begin{cases} \dfrac{T_{exp}}{T_M} & \text{if } \dfrac{T_{exp}}{T_M} > 2, \\ \dfrac{\dfrac{T_{exp}}{T_M}}{\dfrac{T_{exp}}{T_M}-1} & \text{if } 1 < \dfrac{T_{exp}}{T_M} < 2, \end{cases} \tag{16}$$

but is this prediction borne out by the data? The results from the zebrafish mutants are encouraging (see Fig. 9(b)). Horikawa et al. (2006) have estimated that M phase of the cell cycle takes at least 15 min, while the somitogenesis clock period is approximately 30 min. This lower bound for the M phase length would yield a spatial frequency of approximately two cell diameters. However, an M phase length of 21 min yields a spatial frequency that is in good agreement with the different mutant autocorrelations. Thus a heuristic argument suggests that an M phase block desynchronisation mechanism could yield a peak in the auto-correlation function that is in qualitative agreement with the Herrgen et al. (2010) measurements. This hypothesis implies that it is not intrinsic stochasticity in the clock dynamics that is responsible for the 'salt and pepper' patterns observed in Delta-Notch and DAPT-treated embryos. Rather, the desynchronisation results from the pausing of the somitogenesis clock during M phase of the cell cycle and the subsequent inability of neighbouring cells to resynchronise, yielding a forced periodicity in the oscillator phase distribution, as described by Eq. (16). The quantitative prediction given by Eq. (16) could be verified experimentally by perturbing the length of M phase of the cell cycle in DAPT-treated embryos and calculating autocorrelation functions.

Whilst the proposed M phase block hypothesis is independent of the particular form of the clock and wavefront model under consideration, we can demonstrate that the phase coupled model proposed in this study can reproduce the peaked autocorrelation functions observed *in vivo*. In order to mimic the phase difference imposed by cell proliferation in the posterior-most PSM, Eq. (3) has been simulated with the boundary condition (15), representing an M phase block induced phase lag in the posterior PSM, imposed on a boundary moving with velocity $\sqrt{\omega B}$ that corresponds to the posterior-most tip of the PSM. This, admittedly coarse, approximation is equivalent to assuming that cell proliferation occurs only on the posterior boundary rather than throughout the PSM. However, it can be justified, to a certain extent, by noting that the induced phase

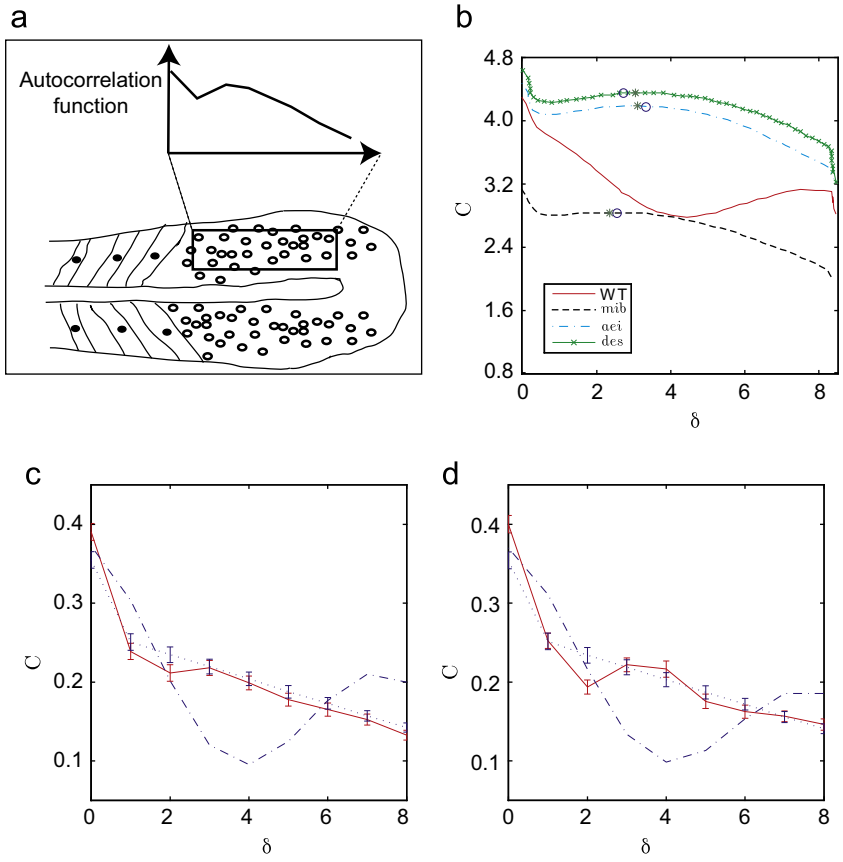

Fig. 9. Autocorrelation functions, $C(\delta)$, plotted against δ. (a) A schematic illustration of autocorrelation calculations. (b) Experimental data: autocorrelation functions from wild-type (solid line) and mutant embryos (Herrgen et al., 2010). Positions of predicted maxima (Eq. (16), circles) are compared with measured maxima (crosses) for an M phase length of 21 min. (c) The autocorrelation function from a simulation of the noise driven desynchronisation hypothesis (solid line) is compared with that from a wild-type pattern (dot-dashed line) and a random phase distribution (dotted line). (d) The autocorrelation function from a simulation of the cell proliferation-driven desynchronisation hypothesis (solid line) is compared with that from a wild-type pattern (dot-dashed line) and a random phase distribution (dotted). Error bars denote standard errors.

lag will be maximal in the posterior PSM where the clock oscillation rate is largest. In the anterior PSM the clock oscillation rate slows significantly, hence the phase-lagging effect of M phase block will be progressively reduced. The resulting autocorrelation function is presented in Fig. 9(d).

Discussion

The relatively recent discovery in multiple vertebrate species of the somitogenesis clock and molecular gradients along the AP axis provides strong evidence for the clock and wavefront mechanism of somitogenesis. In the classical interpretation of the model, the wavefront and the clock determine where and when somite formation occurs, respectively, with somite length predicted to be related to the clock period via the relationship $S_{exp} = vT_{exp}$. However, in recent experiments in zebrafish, the wavefront velocity is measured to be unchanged while the ratio of somite length to clock period varies between the different mutants.

Herrgen et al. (2010) quantified spatial autocorrelation in the posterior PSMs of a range of zebrafish mutant embryos, allowing the quantitative comparison of 'salt and pepper' patterns across different mutant embryos. Intriguingly, they have found a peak in the autocorrelation function at a wavelength of approximately four cell diameters. It is not well understood what mechanisms could give rise to the observed spatial patterning.

We have recently developed a new variation of the clock and wavefront model in which a system of phase coupled oscillators, where the coupling behaviour is resolved into two distinct types that are at least partially mediated by Delta-Notch signalling, is sufficient to explain a range of observations of zebrafish somitogenesis. Whilst the previous work proposed a generic mechanism for somitogenesis and was parameterised in a number of different species, the aim of the current study is to apply the model to recent observations in zebrafish and, consequently, make testable predictions (see Fig. 10) that can be validated in future experiments.

In the Hes6 mutant embryo, the wavefront velocity has been measured to be unchanged and somite length increases (relative to wild-type) proportionally with somitogenesis period, a result that is consistent with the classical interpretation of the clock and wavefront model. This observation can be accounted for in our model if the repulsive coupling strength increases in proportion with the (observed) decrease in oscillation frequency. We speculate that this effect could simply be accommodated by competition for Hes6 binding. For example, suppose that a complex X can exist in an unbound state where it activates repulsive coupling and in a complex with Hes6 where it accelerates the clock. Removal of Hes6 would result in a slowing of the clock and an increase in repulsive coupling, in agreement with the experimental observations.

Herrgen et al. (2010) used two measurements of pattern wavelength in the anterior PSM: somite and segment length. Upon consideration of the more anterior somite length measurements, none of the Delta-Notch mutants satisfy the relationship

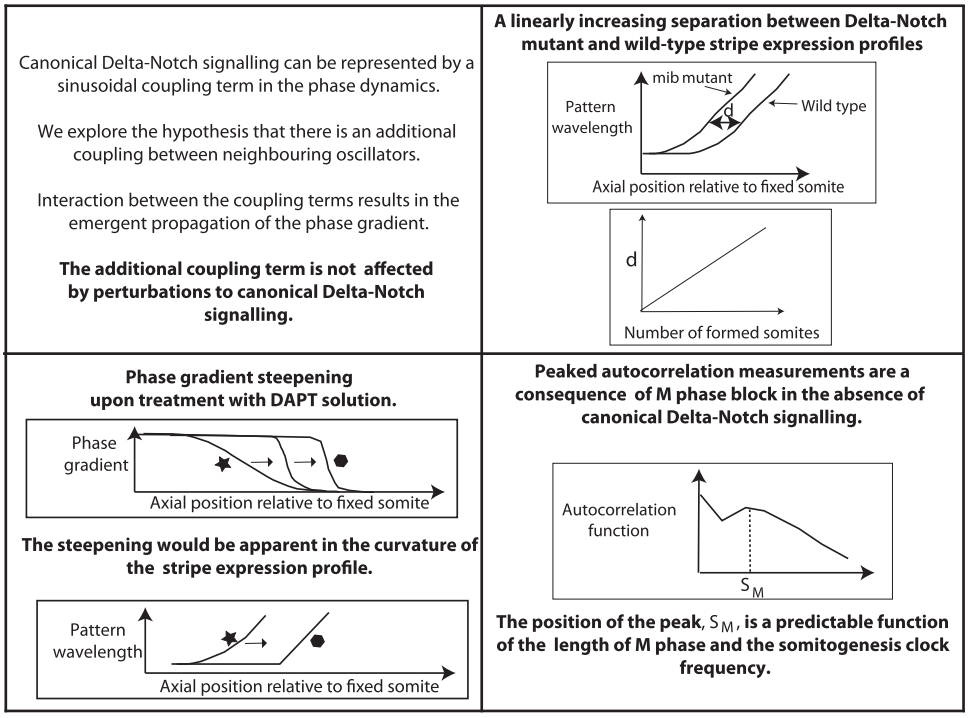

Fig. 10. A schematic illustration of testable model predictions.

$S_{exp} = vT_{exp}$. Moreover, the DAPT-treated, *aei* and *mib* embryos are grouped together and do not display a significant change in repulsive coupling strength. We suggest that the *des* mutant does not lie with the other Delta-Notch mutants because the notch1a receptor is used to mediate repulsive oscillator coupling via noncanonical Delta-Notch signalling.

Analysis of our model suggests that the somite length measurement is favourable over the segment length for the following reasons: when using the somite length data: (a) the *mib*, *des* and DAPT-treated embryos group together; (b) the parameter B is independent of canonical Delta-Notch signalling, thus allowing the Delta-Notch mutants to be modelled by changing the parameters A and ω; and (c) the phase gradient velocity is consistent with a least squares fit of our model to the *mib* stripe expression data. Although the somite measurements lead to the conclusion of a reduced phase gradient velocity that is consistent with *mib* expression profiles, we highlight that Herrgen et al. (2010) measured that the speed of the wavefront, calculated using the position of a gene expression stripe that appears just prior to somite formation (mesp-b) as a proxy for its position, is unchanged in the different Delta-Notch mutant embryos. How can these two opposing viewpoints be reconciled? We suggest that the prediction of a reduced phase gradient velocity can be married to experimental observations if the phase gradient can move independently of the mesp-b stripes in the mutant embryos, *i.e.* a prediction of the model is that the phase gradient slowly drifts out of synchrony with the unchanged global growth rate of the mutant embryos. We highlight that the prediction of a reduced phase gradient velocity in Delta-Notch mutants can be validated using real-time expression assays.

In a classical interpretation of Cooke and Zeeman's clock and wavefront model, the wavefront moves independently of the clock. Thus, upon removal of synchronising coupling, the cellular oscillators desynchronise and, eventually, the spatiotemporal patterning that precedes somitogenesis is completely disrupted. In this model ALD is a measure of the time taken for the effects of noise to gradually accumulate in the posterior PSM.

In our model the wavefront is an emergent phenomenon that arises as a result of the combination of repulsive and attractive coupling. A complete cessation of both repulsive and attractive coupling would result in the instantaneous stalling of the wavefront. However, upon disruption of just diffusive coupling ($A=0$), the nonlinear (repulsive coupling) term dominates and the phase gradient steepens until the wavefront eventually stalls, thus providing a mechanism for the delayed formation of somites upon removal of diffusive coupling. However, the continuum model predicts the formation of approximately six somites which is five somites fewer than the experimentally observed value. We have suggested a number of factors that might contribute towards the underestimate and highlighted that the analysis of real-time expression patterns of DAPT-treated zebrafish embryos will allow the phase gradient steepening hypothesis to be experimentally validated.

A further consideration to take into account when trying to relate the phase-coupled model to experimental data is that complexes which mediate communication between neighbouring oscillators could change on much slower time scales than the concentration of individual molecules. Therefore, although Özbudak and Lewis (2008) have placed a 60 min upper bound on the time for DAPT to penetrate into PSM cells, it may be the case that phase diffusion (i.e. the parameter A) is disrupted on a much longer time scale. Hence, somites that form beyond the six predicted by the continuum model could at least partially arise as a result of a delay in the perturbation of the phase parameters. Whilst such a delay might be measurable experimentally, it could only be fully theoretically understood by relating the phase model parameters A, B and ω to models for the underlying molecular networks that control clock oscillations and oscillator coupling. As discussed in Murray et al. (2011), it is theoretically possible to derive Eq. (4) from an underlying molecular-level model of the segmentation clock network. This would provide a direct between the gene regulatory network of the clock and the characteristics of the spatial pattern and allow us to make further predictions from our model.

In order to investigate whether intrinsic transcriptional noise could yield agreement with the peaked autocorrelation measurements made by Herrgen et al. (2010) in Delta-Notch mutant embryos, we introduced a Gaussian noise term that represented noise in the somitogenesis clock to our description of the phase dynamics. We found that, upon removal of synchronising coupling, a combination of noise and repulsive coupling desynchronises oscillators in the posterior PSM and the propagation of pattern is halted. Thus our model simulations were broadly consistent with the desynchronisation hypothesis. However, the introduction of a Gaussian noise term, perhaps expectedly, resulted in autocorrelations that were not in agreement with the Herrgen et al. (2010) measurements.

In order to explain the peak of the autocorrelation function in Delta-Notch mutants, we have examined an alternative hypothesis in which the pausing of the somitogenesis clock during M phase of the cell cycle forces phase distributions in the posterior PSM to have a characteristic frequency. This hypothesis can explain qualitative features of the autocorrelation function in mutant embryos. Moreover, assuming that the length of M phase of the cell cycle is unaltered in the Delta-Notch mutants, variation in the position of the peaks of the autocorrelation functions in the different mutants might be accounted for by the measured differences in somitogenesis periods. However, we note that if cell proliferation plays a role in the patterns observed in the PSM of mutant embryos, biophysically realistic models of cell proliferation and movement and how they couple to oscillator phase dynamics will be required in order to explain the quantitative variation in the ALD in the Delta-Notch mutants. This topic will be investigated in a future study.

The keen reader will have noted a logical flaw in our description of ALD in Delta-Notch mutant embryos: the model requires the presence of an initial phase gradient and it is not clear how this could be set up if the synchronising coupling strength was always zero. Answering this question is beyond the scope of this paper as we believe that the solution requires a detailed understanding of the first clock cycles that occur along the vegetal boundary of the blastoderm upon formation of the germ ring (Riedel-Kruse et al., 2007; Ishimatsu et al., 2010), and of cell movements that occur as gastrulation, epiboly and involution proceed (Warga and Kimmel, 1990). However, we speculate that there is the potential for the formation of an initial phase gradient as cells undergoing involution and convergent extension are actively moving through the oscillating region of the blastoderm and, thus, could record a spatio-temporally varying signal that might specify the initial phase gradient.

In summary, we have recently proposed a generic clock and wavefront model of somitogenesis in which the wavefront that slows the clock oscillation rate along the AP axis is an emergent function of oscillator coupling. In the current study we apply the model to a range of measurements taken from zebrafish and make a number of predictions that will be testable using real-time expression assays. The validation of the proposed model predictions in future experiments would add strong support to the hypothesis that, as well as synchronising neighbouring oscillators, coupling plays a role in the slowing of oscillations along the AP axis.

Acknowledgment

PJM and REB acknowledge the support of the Engineering and Physical Sciences Research Council through an EPSRC First Grant to REB. PKM was partially supported by a Royal Society-Wolfson Research Merit Award. PJM acknowledges the support of St Hugh's College, Oxford and the OCISB project (BB/D020190/1).

Appendix A. An outline of the model derivation and relevant solutions

The steady-state phase difference in Eq. (3) is

$$\Delta\theta = \cos^{-1}\left(1-\frac{\omega}{2B}\right) = \sqrt{\frac{\omega}{B}}\left(1+\frac{\omega}{24B}+O\left(\left(\frac{\omega}{2B}\right)^2\right)\right), \tag{17}$$

while ahead of the wavefront $\theta=\omega t$. Upon taking the continuum limit of Eq. (3), we obtain the partial differential equation (PDE)

$$\frac{\partial\theta}{\partial t} = \omega + A\cos\left(\frac{\partial\theta}{\partial x}\right)\frac{\partial^2\theta}{\partial x^2} + 2B\left(\cos\left(\frac{\partial\theta}{\partial x}\right)-1\right), \tag{18}$$

where $\theta(x,t)$ is the phase distribution along the AP axis at time t. Making the further assumption that neighbouring oscillators are close together in phase, *i.e.* $|\theta_i-\theta_{i-1}| \ll 2\pi$, and Taylor expanding the sine and cosine terms in Eq. (18) about zero we obtain the leading order equation (Murray et al., 2011)

$$\frac{\partial\theta}{\partial t} = \omega + A\frac{\partial^2\theta}{\partial x^2} - B\left(\frac{\partial\theta}{\partial x}\right)^2. \tag{19}$$

We note that, although the steady-state of Eq. (4) ($\sqrt{\omega/B}$) appears at leading order of Eq. (17), the correction term is approximately 4% for wild-type zebrafish parameters (see Table 2), a discrepancy that arises as a result of the truncated Taylor expansions of the sine and cosine functions.

The relatively simple form of Eqs. (19) and (5) has the consequence that it is possible to derive an expression for the phase gradient given by

$$\Psi(x,t) = \frac{\sqrt{\omega/B}}{1+\exp\left(\frac{\sqrt{\omega B}}{A}(x-vt)\right)}, \tag{20}$$

where the wave speed $v=\sqrt{\omega B}$ and $\Psi=\partial\theta/\partial x$ denotes the phase gradient. The pattern wavelength, a readily measurable quantity, is given by

$$S(x,t) = 2\pi\sqrt{\frac{B}{\omega}}\left(1+\frac{A}{\pi B}\sinh^{-1}\left(\sinh\left(\frac{\pi B}{A}\right)\exp\left(\frac{\sqrt{\omega B}(x-vt)}{A}\right)\right)\right). \tag{21}$$

Appendix B. Phase gradient steepening

Assuming that at $t=t_0$ the phase gradient is initially given by $\Psi_0(x)=\Psi(x,t=t_0)$, we disrupt synchronising coupling by setting $A=0$ and the governing equation for the phase gradient, found by differentiating Eq. (4) with respect to x, is given by

$$\frac{\partial\Psi}{\partial t} + 2B\Psi\frac{\partial\Psi}{\partial x} = 0. \tag{22}$$

Assuming $\Psi_0(x)$ is a decreasing function of x, it can be shown, using the method of characteristics, that the phase gradient develops a singularity after a time

$$t_s = \frac{1}{2B\max|\Psi_0'(x)|}, \tag{23}$$

where the prime denotes differentiation with respect to x, and the spatial domain eventually splits into two regions: $x<x_0+x_s$, where Ψ takes the value $\sqrt{\omega/B}$ and $x>x_0+x_s$, where $\Psi=0$. Thus, after setting $A=0$ the phase gradient propagates for the finite time t_s, becomes infinitely steep (see Fig. 6(e)) and stalls.

We can use the expression for the time taken for the wavefront to stall to derive an expression for the number of somites that form after the disruption of diffusive coupling. As the wavefront steepens, the centre point of the phase gradient ($\Psi=1/2\sqrt{\omega/B}$) continues to move with velocity $\sqrt{\omega B}$ and hence travels a

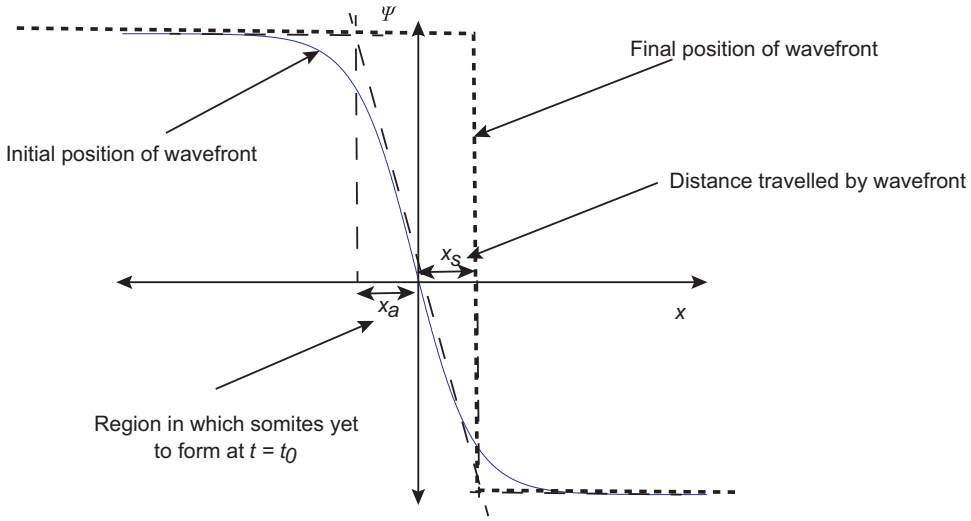

Fig. B1. A schematic illustration of the steepening wavefront in Ψ.

distance

$$x_s = \sqrt{\omega B}t_s = \frac{\sqrt{\omega B}}{2B\max|\Psi_0'(t_0)|}, \tag{24}$$

before the wavefront stalls. Whilst the distance travelled by the centre of the phase gradient, x_s, could, in principle, be experimentally measured and compared with Eq. (24), if we wish to use the ALD data we must relate our model for pattern propagation to somite formation (see schematic in Fig. B1), *i.e.* we need to know how many somites are morphologically observable at $t = t_0$ in order to be able to count how many somites form after the perturbation. As somite formation does not occur until the moving stripes of gene expression have come to rest, *i.e.* $\Psi \to \sqrt{\omega/B}$ in our model, we use a linear approximation to the phase gradient at $t = t_0$ to estimate x_a, the length of the region of the PSM anterior to the centre of the phase gradient which will yield further somites, and obtain

$$x_a = \frac{\sqrt{\omega/B}}{2\max|\Psi_0'(x_0)|}. \tag{25}$$

Hence, after disrupting synchronising coupling at $t = t_0$, a length of the PSM measuring $x_a + x_s$ will yield a further

$$N_s = \frac{x_a + x_s}{S_{exp}} = \frac{\sqrt{\omega/B}}{\max|\Psi_0'(x_0)|S_{exp}}, \tag{26}$$

somites before the wavefront stalls. We highlight that a precise measurement of Ψ at the instant when diffusive coupling is disrupted is necessary to quantitatively validate our model against the ALD data. As such, the simplest case in which to validate the prediction made in Eq. (26) is when the embryo has already generated a sufficient number of somites such that the phase gradient is in dynamic equilibrium and hence given by Eq. (20). In this limiting case we obtain that

$$\max|\Psi_0'| = \frac{\omega}{4A}, \tag{27}$$

hence

$$N_s = \frac{4A}{\sqrt{\omega B}} = \frac{L_{exp}}{S_{exp}}. \tag{28}$$

We note that as the phase gradient becomes increasingly steep, the length scale over which it varies from $\sqrt{\omega/B}$ to zero decreases (see Fig. 6(e)). However, as the length scale of the phase gradient approaches that of a single cell, we expect that the continuum model is no longer a valid description of cellular phase dynamics. In the solution of the discrete model (Eq. (1)) with $A = 0$, the phase gradient steepens, as in the continuum case, as $t \to t_s$. At $t > t_s$, the spatial domain separates into two distinct regions: anteriorly, the pattern wavelength is approximately S_{exp}, while posteriorly it is zero. However, for $t > t_s$ the discrete model behaviour differs from the continuum case, as the wavefront does not stall but continues to propagate posteriorly (see Fig. 7). Hence the discrete nature of the oscillators in the limit of a steepening wavefront permits the formation of further pattern segmentation after the breakdown of the continuum model.

The discrete model in the absence of attractive coupling

Defining $\Psi_j = \theta_j - \theta_{j-1}$, the governing equation for the phase differences in the absence of synchronising coupling ($A = 0$) can be shown, upon manipulation of Eq. (3), to be

$$\frac{d\Psi_j}{dt} = B(\cos(\Psi_{j+1}) - \cos(\Psi_{j-1})). \tag{29}$$

Thus the phase differences attain steady state values when $\Psi_{j+1} = \pm\Psi_{j-1}$ and propagate from the posterior boundary of the PSM. Hence, if one was to induce a phase difference of $\Delta\theta$ in the posterior-most PSM, the repulsive coupling term could allow that phase difference to propagate through the posterior PSM.

References

Aulehla, A., Wiegraebe, W., Baubet, V., Wahl, M.B., Deng, C., Taketo, M., Lewandoski, M., Pourquié, O., 2008. A β-catenin gradient links the clock and wavefront systems in mouse embryo segmentation. Nat. Cell. Biol. 10, 186–193.

Baker, R.E., Schnell, S., Maini, P.K., 2008. Mathematical models for somite formation. Curr. Top. Dev. Biol. 81, 183–203.

Bénazéraf, B., Francois, P., Baker, R.E., Denans, N., 2010. A random cell motility gradient downstream of FGF controls elongation of an amniote embryo. Nature 466, 248–252.

Cooke, J., Zeeman, E.C., 1976. A clock and wavefront model for control of the number of repeated structures during animal morphogenesis. J. Theor. Biol. 58, 455–476.

Geling, A., Steiner, H., Willem, M., Bally-Cuif, L., Haass, C., 2002. A γ-secretase inhibitor blocks Notch signaling in vivo and causes a severe neurogenic phenotype in zebrafish. EMBO Reports 3, 688–694.

Gilbert, S.F., 1997. Developmental Biology. Sinauer Associates, 5th edn.

Giudicelli, F., Özbudak, E.M., Wright, G.J., Lewis, J., 2007. Setting the tempo in development: an investigation of the zebrafish somite clock mechanism. PLoS Biol. 5, e150.

Goldbeter, A., Pourquié, O., 2008. Modeling the segmentation clock as a network of coupled oscillations in the Notch, Wnt and FGF signaling pathways. J. Theor. Biol. 252, 574–585.
Herrgen, L., Ares, S., Morelli, L.G., Schröter, C., Jülicher, F., Oates, A.C., 2010. Intercellular coupling regulates the period of the segmentation clock. Curr. Biol. 20, 1244–1253.
Hirata, H., Yoshiura, S., Ohtsuka, T., Bessho, Y., Harada, T., Yoshikawa, K., Kageyama, R., 2002. Oscillatory expression of the bHLH factor Hes1 regulated by a negative feedback loop. Science 298, 840–843.
Horikawa, K., Ishimatsu, K., Yoshimoto, E., Kondo, S., Takeda, H., 2006. Noise-resistant and synchronized oscillation of the segmentation clock. Nature 441, 719–723.
Ishimatsu, K., Takamatsu, A., Takeda, H., 2010. Emergence of traveling waves in the zebrafish segmentation clock. Development 137, 1595–1599.
Jiang, Y.J., Aerne, B.L., Smithers, L., Haddon, C., Ish-Horowicz, D., Lewis, J., 2000. Notch signalling and the synchronization of the somite segmentation clock. Nature 408, 475–479.
Kærn, M., Menzinger, M., Hunding, A., 2000. Segmentation and somitogenesis derived from phase dynamics in growing oscillatory media. J. Theor. Biol. 207, 473–493.
Kawamura, A., Koshida, S., Hijikata, H., Sakaguchi, T., Kondoh, H., Takada, S., 2005. Zebrafish hairy/enhancer of split protein links FGF signaling to cyclic gene expression in the periodic segmentation of somites. Gen. Dev. 19, 1156–1161.
Lewis, J., 2003. Autoinhibition with transcriptional delay: a simple mechanism for the zebrafish somitogenesis oscillator. Curr. Biol. 13, 1398–1408.
Lewis, J., Hanisch, A., Holder, M., 2009. Notch signaling, the segmentation clock, and the patterning of vertebrate somites. J. Biol. 8, 44.
Masamizu, Y., Ohtsuka, T., Takashima, Y., Nagahara, H., Takenaka, Y., Yoshikawa, K., Okamura, H., Kageyama, R., 2006. Real-time imaging of the somite segmentation clock: revelation of unstable oscillators in the individual presomitic mesoderm cells. Proc. Nat. Acad. Sci. 103, 1313–1318.
Momiji, H., Monk, N.A.M., 2008. Dissecting the dynamics of the Hes1 genetic oscillator. J. Theor. Biol. 254, 784–798.
Morelli, L.G., Ares, S., Herrgen, L., Schröter, C., Jülicher, F., Oates, A.C., 2009. Delayed coupling theory of vertebrate segmentation. HFSP J. 1, 55–66.
Murray, P.J., Maini, P.K., Baker, R.E., 2011. The clock and wavefront model revisited. J. Theor. Biol. 283, 227–238.
Oates, A.C., Ho, R.K., 2002. Hairy/E spl-related Her genes are central components of the segmentation oscillator and display redundancy with the Delta/Notch signaling pathway in the formation of anterior segmental boundaries in the zebrafish. Development 129, 2929–2946.
Özbudak, E.M., Lewis, J., 2008. Notch signalling synchronizes the zebrafish segmentation clock but is not needed to create somite boundaries. PLoS Genet. 4, e15.
Palmeirim, I., Henrique, D., Ish-Horowicz, D., Pourquié, O., 1997. Avian hairy gene expression identifies a molecular clock linked to vertebrate segmentation and somitogenesis. Cell 91, 639–648.
Riedel-Kruse, I.H., Muller, C., Oates, A.C., 2007. Synchrony dynamics during initiation, failure, and rescue of the segmentation clock. Science 317, 1911–1915.
Schröter, C., Oates, A.C., 2010. Segment number and axial identity in a segmentation clock period mutant. Curr. Biol. 20, 1254–1258.
Soroldoni, D., Oates, A.C., 2011. Live transgenic reporters of the vertebrate embryo's segmentation clock. Curr. Opin. Gen. Dev. 21, 600–605.
Strogatz, S.H., 2000. From Kuramoto to Crawford: exploring the onset of synchronization in populations of coupled oscillators. Physica D 143, 1–20.
Van Eeden, F.J., Granato, M., Schach, U., Brand, M., Furutani-Seiki, M., Haffter, P., Hammerschmidt, M., Heisenberg, C.P., Jiang, Y.J., Kane, D.A., Kelsh, R.N., Mullins, M.C., Odenthal, J., Warga, R.M., Allende, M.L., 1996. Mutations affecting somite formation and patterning in the zebrafish *Danio rerio*. Development 123, 153–164.
Warga, R.M., Kimmel, C.B., 1990. Cell movements during epiboly and gastrulation in zebrafish. Development 108, 569–580.
Winfree, A.T., 1967. Biological rhythms and the behavior of populations of coupled oscillators. J. Theor. Biol. 16, 15–42.